Received: 5 April 2017 | Revised: 5 June 2017 | Accepted: 11 June 2017

DOI: 10.1002/er.3806

RESEARCH ARTICLE

WILEY INTERNATIONAL JOURNAL OF ENERGY RESEARCH

Experimental study and analytical modeling of an alkaline water electrolysis cell

Yanan Chen[1,2] | Felipe Mojica[1] | Guangfu Li[1] | Po-Ya Abel Chuang[1]

[1] Department of Mechanical Engineering, University of California, 5200 North Lake Road, Merced, CA 95343, USA

[2] State Key Laboratory of Advanced Technology for Materials Synthesis and Processing, Wuhan University of Technology, Wuhan 430070, China

Correspondence
Po-Ya Abel Chuang, Department of Mechanical Engineering, University of California, 5200 North Lake Road, Merced, CA 95343, USA.
Email: abel.chuang@ucmerced.edu

Summary

A traditional alkaline aqueous electrolyzer is investigated by using a 3-electode structure that enables the reaction resistance of each individual electrode to be accurately monitored. Combining experimental observations with resistance-based model analysis, we establish a quantitative relationship between current density and key voltage losses, including losses due to thermodynamics, kinetics, ohmic, and mass transport. These results demonstrate that the oxygen evolution reaction and bubble effects play crucial roles in determining electrolyzer performance. By varying the distance between electrodes, 2 effective OH^- conductivities in 0.4M KOH are found to be 0.1333 and 0.9650 second cm^{-1}, depending on bubble formation and release rate at the electrode interface. Moreover, bubble coverage on electrode surface achieves a steady state of 96% when current density is above 0.1 A cm^{-2}. In the study of various electrolyte concentrations, all the model predictions show good agreement with experimental results, confirming its ability to capture actual cell performance. This newly presented empirical resistance-based model provides a practical framework to simulate complicated electrolysis reactions, serving as a comprehensive guide for continuous improvement of water electrolysis.

KEYWORDS

analytical model, hydrogen energy, oxygen evolution reaction, water electrolysis

1 | INTRODUCTION

Water electrolysis (WE) is a promising and clean technology that has an advantage over other renewable energy sources (like solar and wind energies) that are stored in the form of hydrogen and, therefore, has attracted increasing research interest in recent years.[1-3] However, the challenges for widespread use of WE are to improve its efficiency and reduce the cost and energy consumption.[1,4] Compared to solid polymer electrolyte WE, the traditional liquid alkaline WE possesses the advantages of long historical development, low cost, and long-term stability.[4-7] In general, this setup consists of an anode, a cathode, liquid electrolyte solution, and a direct current (DC) power supply. However, with the system of 2 electrodes, it is difficult to study a half reaction occurring at an electrode (called working electrode, WE). To address this issue, one standardized method is to introduce a reference electrode (RE) into the electrolysis cell with which WE potential can be directly controlled or detected.[8]

The reversible voltage (E_{rev}) needed to split a water molecule into hydrogen, and oxygen can be determined by the Gibbs free energy.[1,5] However, the applied voltage during realistic operation is generally much higher than E_{rev} due to over-potential losses.[9,10] The losses caused by hydrogen evolution reaction (HER) and oxygen evolution reaction (OER) strongly depend on electrode materials, operating conditions, and the electrolyzer.[10] Moreover, the formation of gas bubbles, especially at high current densities, will require higher energy to sustain the same corresponding reaction rate.[7,11]

The characterization of the main voltage components and gas bubble behavior in WE is crucial in understanding experimental phenomena and optimizing operating system and control strategies. In addition to experimental observations, there have been numerous simulation efforts to address the fundamental issues of WE.[4,6,12] In early modeling studies,[13-15] the approaches applied were limited only to their electrolysis systems. Recent model development has made significant progress, as described in recent review articles.[12,16,17] However, most of the reported work applied a simple resistance-based model for determining energy consumption. Little work was supported by experimental observations. This is particularly an issue since most models do not account for the effect of gas bubbles, which experiments have shown to be important. Based on this, it has been noted that the development of computational modeling is still far behind the current state of WE technology.[4]

Herein, combining experimental observations and modeling results, we establish a quantitative relationship between each voltage component and current density, which includes all resistances in the alkaline water electrolyzer. A 3-electrode system built with a defined-potential RE allows us to monitor the anode and cathode reactions separately. In particular, the effect of gas bubbles on kinetic and transport resistances is quantified based on the experimental data.

2 | EXPERIMENTAL METHODS

The desktop WE experiment used in this study is illustrated in Figure 1. The platinum wire used as the electrode in anode and cathode has a 0.5 mm diameter and is 5 cm in length with 99.99% trace metals basis. The length of the electrode submerged in the electrolyte is 2 cm, and the effective reaction surface area is calculated to be 0.316 cm^2. Potassium hydroxide (KOH, Sigma-Aldrich, ≥ 90 wt%) solution, which is most commonly used in alkaline WE due to its high conductivity,[18] is used as the electrolyte for our experiment. A baseline of 0.4M of KOH concentration is used, but 0.2M and 1M are also tested to compare with the modeling data. We install a mercury/mercury oxide (Hg/HgO) RE, which is the most widely used RE with a stable potential in alkaline electrolyte,[19] to survey the voltage between the cathode and RE. It should be noted that the cathode reversible- and over-potentials shown in this work refer to their absolute values. The pH of KOH solution is measured to be 13.93 at 25°C. The RE potential at 25°C and pH = 14 is 0.0984 V vs standard hydrogen electrode (SHE).[20] Therefore, the corrected RE potential can be calculated as

$$E_{RE} = 0.0984\text{V} + \frac{2.303\times RT}{F}(14-\text{pH}_{\text{RE}}) = 0.1025\ \text{V}. \quad (1)$$

In our study, a DC power supply, BK Precision Model 9130, is used to control and measure voltage and current between working and counter electrodes. In addition, a Gamry Reference 3000 is introduced to measure the potential difference between the cathode and RE. Both current and voltage data acquisition sampling rates are set to be 10 Hz. The cathode potential is measured by the Gamry device directly, while the anode OER potential is calculated from the voltage difference between the power supply and the Gamry device. For this basic WE experiments, there are many control parameters to determine the cell performance. The baseline testing conditions and parameters are listed in Table 1.

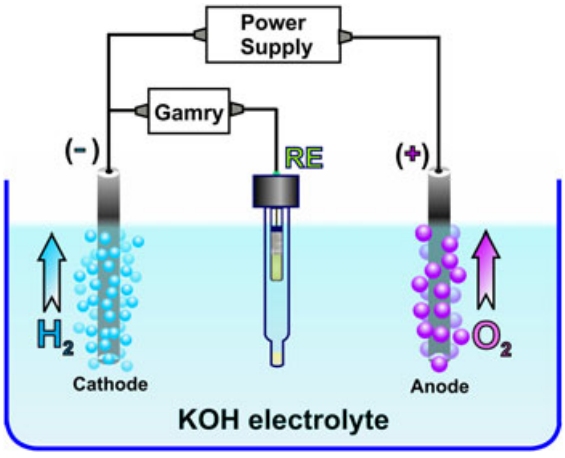

FIGURE 1 Illustration of the desktop water electrolysis experimental setup. RE, reference electrode [Colour figure can be viewed at wileyonlinelibrary.com]

3 | RESULTS AND DISCUSSION

3.1 | Baseline tests

The first step is to study the repeatability and uncertainties of the baseline test and to identify the time required for each test condition to reach steady state. Figure S1 shows 60 seconds of transient voltage data at 6 representative current density settings for the baseline experiment. It can be observed that the voltage signal responds to the current density setting quickly and reaches steady state within

TABLE 1 Experimental baseline settings

No.	Parameter	Setting	Unit
1	Electrolyte volume	200.0	mL
2	Reaction surface area	0.316	cm^2
3	Distance between anode and cathode	1.0	cm
4	Electrolyte concentration	0.4	M
5	Operating temperature	25 ± 1.0	°C

60 seconds for all cases. To be consistent, all steady-state data reported in this study are obtained by averaging the last 10 seconds of the 60-second test duration for each current density set point.

Six repeated baseline tests are performed at the condition settings listed in Table 1. The tests are done by controlling the current output from the DC power supply, and the corresponding total voltages are recorded as shown in Table S1. The mean and standard deviation values are obtained from the 6 measurements, and the percent error is calculated as the standard deviation divided by the average voltage at each current setting. The cathode potential is directly obtained from the measurements of the RE, and the anode potential is simply the difference between the total reaction and cathode reaction. All voltages discussed in this work refer to the potential relative to the SHE.

These averaged baseline results are plotted in Figure 2 to show the polarization *i-V* curve of the total reaction as well as the curves from the individual anode and cathode. The collective results confirm that the total reaction measurements are relatively repeatable and the error percentages are less than 1% throughout the entire range of current densities. The half-cell potentials of HER and OER have slightly higher variation but are both within 2% error. One of the major reasons for the data fluctuation can be ascribed to gas bubbles, which are continuously formed and removed at the reaction interface. This dynamic bubble effect causes a slight variation of the electrode surface area available for reaction. The mean voltage values of the total, cathode, and anode reactions are used throughout this study to derive empirical results for the analytical model described in section 3.3.

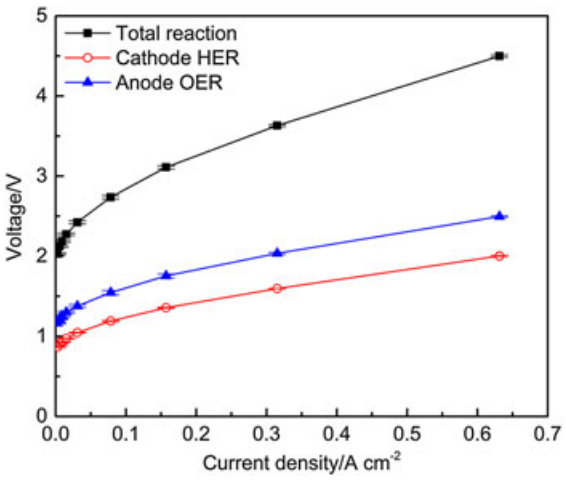

FIGURE 2 Average performance with standard deviation at each current density from 6 repeated tests at the baseline settings. HER, hydrogen evolution reaction; OER, oxygen evolution reaction [Colour figure can be viewed at wileyonlinelibrary.com]

3.2 | Study of electrode distance

Hydroxide transfer to the reaction interface depends on the electrolyte concentration and separation distance between anode and cathode.[21] In principle, ion transport resistance increases with the distance between the anode and cathode. Since there is an abundance of hydroxide in the liquid electrolyte, its exact transport distance is not simply equal to the spacing between anode and cathode, making transport distance difficult to quantify. To investigate the effect of hydroxide transport resistance, the distance between anode and cathode is varied between 1.0 and 2.0 cm.

It can be observed from the reaction polarization plots in Figure 3 that cell voltage increases with electrode spacing, indicating an increase of ion transport resistance. This is consistent with early observation in the literature.[21] The cathode and anode half-cell voltage in the 3-electrode setup can also be measured and are reported in Figure 3B,C, respectively. These results are used to obtain ion transport resistances during operation.

3.3 | Development of analytical model

A 1-D analytical model is developed to evaluate the relative effects of the major overpotentials, including the thermodynamics of WE, kinetics of HER and OER, ohmic resistances for electron and hydroxide transport, and mass transport losses due to bubble formation. The actual cell potential (E_{cell}) can be calculated by the combination of reversible

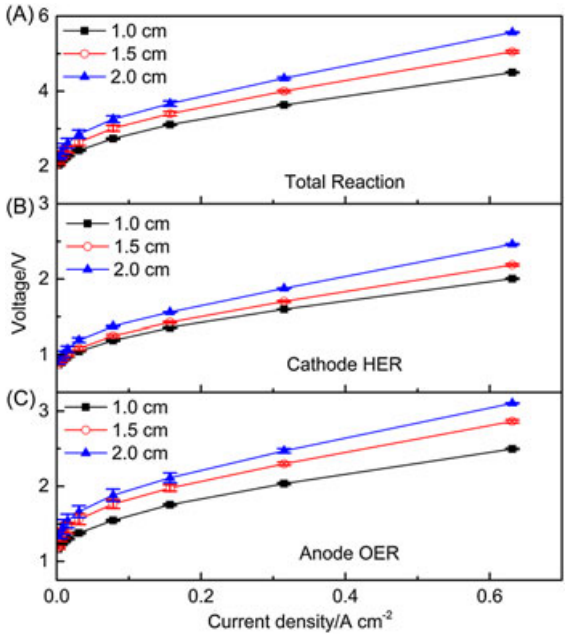

FIGURE 3 Polarization curves of total, anode, and cathode reactions at various electrode distances. The error bar represents the standard deviation of 6 repeating tests [Colour figure can be viewed at wileyonlinelibrary.com]

potential (E_{rev}), activation over-potential for HER (η_{HER}) and OER (η_{OER}), electron transport resistance (R_{e^-}), hydroxide transport resistance (R_{OH^-}), and voltage loss due to mass transport (η_{mx}). The sum of overall cell potential found in a typical electrolysis system can be expressed as

$$E_{cell} = E_{rev} + \eta_{OER} + |\eta_{HER}| + i\times(R_{e^-} + R_{OH^-}) + \eta_{mx}. \quad (2)$$

In the following sections, we will discuss each term in detail.

3.3.1 | Equilibrium potential

The amount of electrical energy required to activate the reaction can be determined from thermodynamic properties, including enthalpy, entropy, and Gibbs free energy (ΔG) of the reactants and products. Under the standard conditions, the reversible cell voltage (E^o_{rev}) can be calculated by a well-known Nernst equation[1,8,22]:

$$E^o_{rev} = -\frac{\Delta G^o}{nF}, \quad (3)$$

where n is the number of electron transfer and F is Faraday' constant (96 485 C mol^{-1}). The equilibrium potential, which is independent of the catalyst material, is a strong function of pressure and temperature and is usually approximated by the combination of Nernst equation and Gibbs free energy, respectively[8,22]:

$$E_{rev} = E^o_{rev} + \frac{\Delta S}{2F}(T - T_0) + \frac{RT}{2F}\ln\left(\frac{a_{H_2}a^{0.5}_{O_2}}{a_w}\right), \quad (4)$$

where R is the Universal Gas Constant and a_i is the activity of species i. In our experiment, the temperature is controlled to be at the reference temperature, and the activity of water (a_w) is equal to 1 due to high water content in the electrolyte. In addition, the pressure of the generated hydrogen and oxygen can be approximated as the atmospheric pressure because the bubbles are close to the liquid surface. Therefore, the activities of hydrogen and oxygen are also equal to 1. Based on these assumptions, the reversible potential of our experiment is equal to 1.228 V. The same analysis for reversible potential can also be applied to HER and OER half reactions. Based on our operating parameters, the equilibrium potentials for HER and OER are calculated to be −0.797 and 0.431 V, respectively.

3.3.2 | Ohmic resistances

The resistances discussed in this section include electronic resistance (R_{e^-}) and ionic resistance (R_{OH^-}) between anode and cathode. These two resistances are referred to as ohmic resistance because the voltage required to drive the electronic and ionic flux can be described by Ohm's law. The electronic resistance can be determined by the electrical conductivity of the used materials and their interface resistances. In the WE system, it is observed that the voltage loss due to R_{e^-} is less than 1 mV even at the studied highest current density. Therefore, it can be neglected in our model analysis.

As discussed earlier, the ionic resistance is a function of the distance between electrodes and the ionic conductivity. Since the distance between 2 electrodes (1 cm) is much greater than the electrode diameter (0.05 cm), a 1-D assumption was made to simplify the geometry. The ionic resistance can be approximated as

$$R_{OH^-} = \frac{d}{K^{eff}_{OH^-}}, \quad (5)$$

where d is the distance between anode and cathode and $K^{eff}_{OH^-}$ is the effective hydroxide ionic conductivity (second cm^{-1}). It is important to note that $K^{eff}_{OH^-}$ is different from the bulk conductivity of a homogeneous aqueous solution[22] and can only be obtained empirically. To further investigate effective hydroxide ionic conductivity, we assume that changing electrode distance results in only the alternation of R_{OH^-} in Equation 2. Therefore, the voltage difference between 2 varied electrode spacings can be written as

$$\Delta E_{cell} = i\times\left(\frac{\Delta d}{K^{eff}_{OH^-}}\right). \quad (6)$$

The collected data for the 3 electrode spacing presented in Figure 3 are further processed to establish the relationship between the cell voltage and electrode distance. The linear relationship observed in Figure 4A confirms the above assumption to be valid. In addition, the slope represents the ratio of $(\Delta E_{cell}/\Delta d)\left(\frac{\Delta E_{cell}}{\Delta d}\right)$ at each current density.

To continue the analysis, we assume that $K^{eff}_{OH^-}$ is not a strong function of the operating current density within a certain range. Equation 6 can be rearranged to present the effective hydroxide ionic conductivity as

$$K^{eff}_{OH^-} = \frac{\Delta i}{\Delta\left(\frac{\Delta E_{cell}}{\Delta d}\right).} \quad (7)$$

According to Equation 7, the slopes obtained in Figure 4A are plotted against current density as shown in Figure 4B. The fitted results show 2 distinct linear trends, representing $K^{eff}_{OH^-}$, and the transition current density occurs at around 0.0325 A cm^{-2}. The effective hydroxide ionic conductivity can be approximated as 0.1333 second cm^{-1} and 0.9650 second cm^{-1} at the low and high current density, respectively. The results validate our assumption that $K^{eff}_{OH^-}$ is not a strong function of the conducting current density within a certain range. However, it is not clear why the $K^{eff}_{OH^-}$ transitions from low conductivity to high conductivity at around 0.0325 A cm^{-2}.

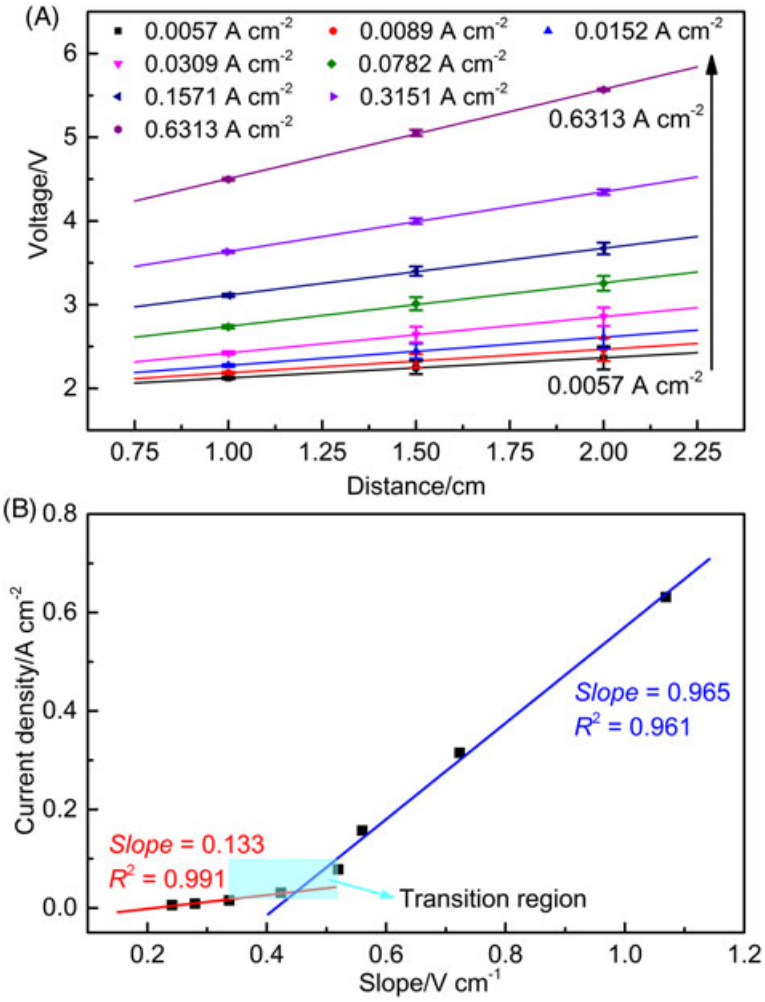

FIGURE 4 A, Cell voltage as a function of electrode distance at various current density; B, corresponding current density as a function of slope [Colour figure can be viewed at wileyonlinelibrary.com]

Upon further study, it is found that the transition current density strongly correlates with bubble formation and release rate at the electrode. During the cell operation period, H_2 and O_2 gas bubbles are generated on the reaction interface of the cathode and anode, respectively. Figure 5 shows pictures of both cathode and cathode electrodes as a function of current density to qualitatively illustrate bubble dynamics. When the current density is below 0.03 A cm^{-2} in our experimental setup, few gas bubbles are observed on the electrode surface, indicating the transport of generation gas occurs primarily through a diffusion mechanism. While the current density is above 0.03 A cm^{-2}, it can be clearly observed from the experiments that gas bubbles are generated and rapidly detached from the reaction sites by buoyancy forces. This bubble flux creates a convective flow of the electrolyte near the electrode, which, in turn, increases the effective hydroxide conductivity.

In the subsequent analytical model, a linear transition from high- to low-effective hydroxide ionic conductivity is used to prevent discontinuity of the ohmic losses. The current densities of the transition region are thus estimated to be between 0.015 and 0.1 A cm^{-2} as marked in Figure 4B.

3.3.3 | Kinetic activation losses

The kinetic activation losses refer to the amount of overpotential required to support and sustain the anode and cathode electrochemical reactions. The governing mechanism can be described by the Butler-Volmer equation, which is applied

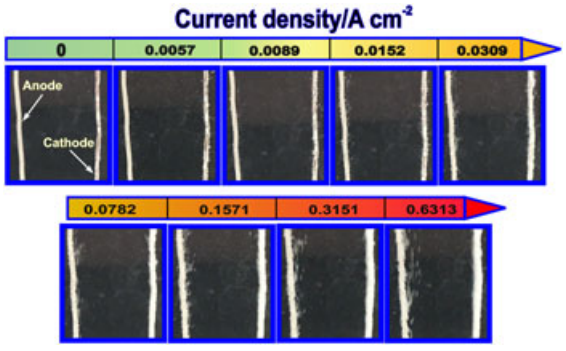

FIGURE 5 Pictures of anode (left) and cathode (right) electrodes at various current density to illustrate bubble dynamics [Colour figure can be viewed at wileyonlinelibrary.com]

to the anode and cathode. The basic Butler-Volmer equation can be written as[8,23]:

$$i = i_0\left(\exp\left(\frac{\alpha nF}{RT}\eta\right) - \exp\left(-\frac{(1-\alpha)nF}{RT}\eta\right)\right), \quad (8)$$

where i_0 is the exchange current density, α is the charge transfer coefficient, and η is the over-potential. The exchange current density, as presented by Equation 9, is a composite parameter, which depends on a rate constant, k^o; reactant and product concentrations, C_O and C_R; and the charge transfer coefficient[24]:

$$i_0 = nFk^o C_{O^{(1-\alpha)}} C_R^{\alpha}. \quad (9)$$

Because the exchange current density is extremely difficult to measure directly, it is often approximated by empirical results at defined reference states, $i_{0(T^*,c_o{}^*,c_R{}^*)}$. With the known exchange current density at standard states, the exchange current density under actual operating conditions can be determined as[24]

$$i_{0(\mathrm{T},c_o,c_R)} = i_{0(T^*,c_o{}^*,c_R{}^*)}\left(\frac{C_R}{C_R{}^*}\right)^{(1-\alpha)}\left(\frac{C_O}{C_O{}^*}\right)^{\alpha} e^{\left(\frac{-E_{\mathrm{act}}^{\mathrm{rev}}}{RT}\times\left(1-\frac{T}{T^*}\right)\right)}, \quad (10)$$

where E_{act}^{rev} is the reaction activation energy.

The standard Butler-Volmer equation given in Equation 8 can be approximated by linear behavior at small over-potential, η, and Tafel behavior at high over-potential. For the alkaline WE study, both HER and OER over-potentials are generally greater than 100 mV due to low exchange current density, i_0, and high reaction current density, i.[25,26] Therefore, the activation over-potential for both HER and OER can be calculated as

$$\eta = b\times\log\left(\frac{i}{i_o}\right) \qquad (\text{for } \eta > 100 \text{ mV}), \quad (11)$$

where $b = \frac{2.303\times RT}{\alpha nF}$ is referred to as the Tafel slope.

The data in Table S1 are processed to obtain the empirical values for the Tafel slopes and exchange current densities for both HER and OER. The reversible potential and the over-potential due to ohmic resistances are subtracted from the cell potential. Only data from low current densities without apparent bubbles forming on the electrode surfaces are used to ensure minimum effect from mass transport losses. The processed over-potentials from HER and OER are plotted in Figure 6. The Tafel slopes and exchange current densities are 80.2 mV dec^{-1} and 4.40E^{-4} A cm^{-2} for HER and 119.6 mV dec^{-1} and 2.32E^{-9} A cm^{-2} for OER, respectively. The calculated results demonstrate that anode OER has slower reaction kinetics compared to cathode HER in the alkaline WE. The main objective of this study is to develop a method for constructing an empirical resistance-based model. It is important to note that the reaction kinetics can be improved by using more active material for OER, ie, IrO_2 and RuO_2[27] or modifying the electrode surface[28] to replace the Pt-wire electrode.

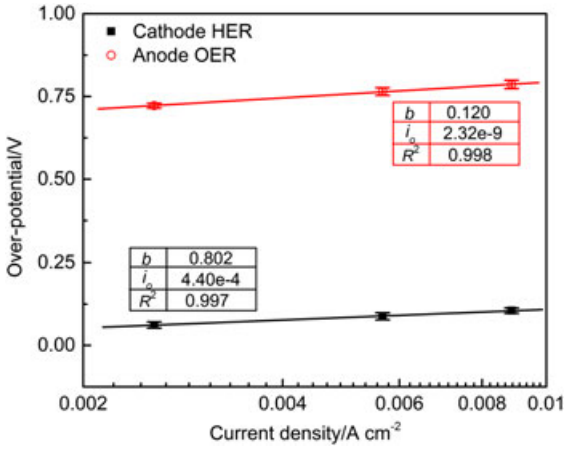

FIGURE 6 Polarization in the kinetic region and the fitted Tafel slopes and exchange current densities obtained from the over-potential data for hydrogen evolution reaction (HER) and oxygen evolution reaction (OER). Symbols, raw data; lines, linear fit to the data [Colour figure can be viewed at wileyonlinelibrary.com]

3.3.4 | Mass transport losses

The mass transport over-potential refers to the performance loss due to the buildup of reactant concentration gradient from the bulk electrolyte to the electrode surface. The reactants in OER and HER are hydroxide and water, respectively. Since liquid water has an activity equal to one, the mass transport over-potential due to liquid water is negligible. The concentration of hydroxide is more complicated and can be calculated from the Nernst-Planck equation, as described below for steady state conditions[24]:

$$J_{\mathrm{OH}^-} = -D_{\mathrm{OH}^-}\nabla C_{\mathrm{OH}^-} - \frac{F}{RT}D_{\mathrm{OH}^-}C_{\mathrm{OH}^-}\nabla\phi + C_{\mathrm{OH}^-}v, \quad (12)$$

where J_{OH^-} is the flux of the hydroxide, D_{OH^-} is the diffusivity of hydroxide in water (a value of 5.273×10^{-5} cm^2 $second^{-1}$ is used in the model),[18] ϕ is the electrolyte potential, and v is the solution stirring velocity. In the baseline experiment, the volumetric hydroxide supply in the solution is calculated to be 4.0e-4 mol cm^{-3} and the reaction rate of hydroxide at the highest current density is calculated to be 6.53e-6 mol cm^{-2} $second^{-1}$. Furthermore, the same amount of hydroxide consumed at the anode is being generated at the cathode side simultaneously. Therefore, no mass transport loss results from hydroxide concentration difference throughout the electrolysis process.

The only transport-related resistances left in the experiment are related to removal of hydrogen and oxygen bubbles. During the cell operation period, H_2 and O_2 gas bubbles are formed and partially cover on the cathode and anode reaction interface, respectively. The size of the bubbles can be calculated by the surface tension, T, and the pressure difference across the meniscus as shown in Equation 13.

$$r_{\text{bubble}} = \frac{4T}{(P_i - P_o)} \tag{13}$$

The liquid pressure, P_o, can be determined by its depth and the density of the fluid (ρ_{fluid}) as shown in Equation 14.

$$P_o = \rho_{\text{fluid}}\, g\, h \tag{14}$$

The bubble release rate (V_{bubble}) is determined by the buoyancy force acting on the bubble, which is directly related to the bubble volume as follows:

$$F_B = \rho_{\text{fluid}}\, V_{\text{bubble}}\, g. \tag{15}$$

As seen in Figure 5, gas bubbles are clearly visible on the electrode surface when the current density is above 0.03 A cm^{-2}. When current density is above 0.07 A cm^{-2}, nearly the entire electrode surface is covered by bubbles. The existence of bubbles on and near the electrode surface has 2 adverse effects on electrochemical reactions. First, the bubbles on the electrode surface block reactants from reaching the catalyst for reaction. Therefore, the available active surface area is reduced and, in turn, the local current density is increased. The magnitude of this increases is based on the bubble coverage, θ. Based on Tafel equation (Equation 11), the effect of bubble coverage on the additional kinetic loss can be calculated as

$$\eta_{\text{mx,kinetic}} = b \times \log\left(\frac{1}{(1-\theta)}\right). \tag{16}$$

Second, the bubbles near the electrode create void space in the electrolyte, which increases hydroxide transport resistance. This mass transport loss phenomenon is a local effect due to the formation of oxygen and hydrogen bubbles, which is different from the bulk effective hydroxide conductivity discussed in the ohmic resistance section. Assuming the bubble coverage percentage on the electrode surface is similar to the void volume percentage in the electrolyte near the electrode, the local hydroxide conductivity can be approximated by Bruggemann correlation.[29] Based on Equation 5, the effect of bubble coverage on the additional local ohmic resistance due to hydroxide transport can be calculated as

$$\eta_{\text{mx,OH}^-} = i \times R^{\text{local}}_{\text{OH}^-} = i \times \frac{d_{\text{bubble}}}{K^{\text{eff}}_{\text{OH}^-}(1-\theta)^{1.5}}, \tag{17}$$

where d_{bubble} is the radial difference between the bubble region and the electrode and is estimated to be 0.2 mm from the pictures in Figure 5. The radius of the local bubble region has a significant impact on overall cell performance, especially under high current density conditions.

To obtain empirical results for the bubble coverage, the HER and OER data in Table S1 are processed to remove kinetic and ohmic losses. The bubble coverage based on Equation 17 is obtained from the residual mass transport losses and is plotted in Figure 7. Although the oxygen generation rate is half that of the hydrogen generation, the data exhibit similar trends of bubble coverage on and near the electrode. This may be due to multiple factors, including bubble size, gas solubility, and gas density, and the effect of these factors could be studied in the future. However, for our empirical-based model, the same correlation for bubble coverage as a function of current density is used for both HER and OER. As observed in Figure 7, bubble coverage grows rapidly at low current densities, ranging from 0 to 0.05 A cm^{-2} and reaches steady-state at around 0.1 A cm^{-2}. These results agree well with the visual observation in Figure 5. In the subsequent analysis, the calculated data points are obtained by fitting the data to the nonlinear equation shown as an inset to Figure 7. The fitted data indicate that the maximum steady-state bubble coverage on the electrode surface is around 95.8%.

3.4 | Comparison of model prediction and experimental data

Considering all the components discussed in the above sections, the electrolysis cell voltage can be approximated as

$$\begin{aligned} E_{\text{cell}} = {} & E_{\text{rev}} + b_{\text{OER}} \log\left(\frac{i}{i_{\text{o,OER}}}\right) + b_{HER} \log\left(\frac{i}{i_{\text{o,HER}}}\right) \\ & + i\left(\frac{d}{K^{\text{eff}}_{\text{OH}^-}}\right) + b_{\text{OER}} \log\left(\frac{1}{1-\theta}\right) + b_{\text{HER}} \log\left(\frac{1}{1-\theta}\right) \\ & + 2\left(i \times \frac{d_{\text{bubble}}}{K^{\text{eff}}_{\text{OH}^-}(1-\theta)^{1.5}}\right). \end{aligned} \tag{18}$$

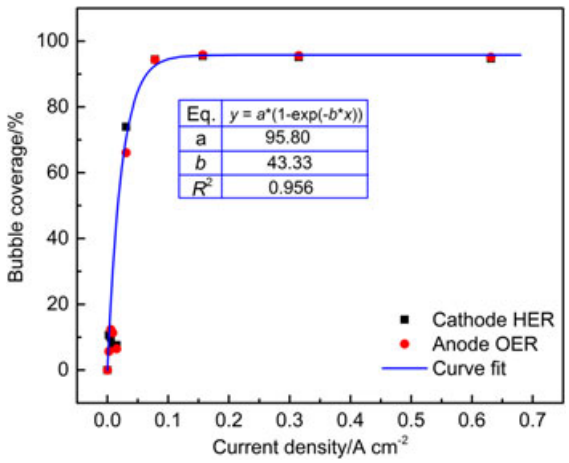

FIGURE 7 Gas bubble coverage calculated from hydrogen evolution reaction (HER) and oxygen evolution reaction (OER) mass transport loses [Colour figure can be viewed at wileyonlinelibrary.com]

All of the parameters discussed in the thermodynamic, kinetic, ohmic, and bubble-induced mass transport analyses are included in the analytical model. The model predicts voltage losses for 5 components, including HER and OER reactions, ohmic resistance, kinetic, and local hydroxide mass transfer. Figure 8A shows that the model predictions are in good overall agreement with the experimental results and that the model captures the correct trends. Voltage losses due to HER and bubble-induced kinetic mass transport have a minor influence on overall cell voltage. The bulk ohmic resistance has a linear relationship with current density. At low current density, OER kinetic loss is the most critical due to its small exchange current density and high Tafel slope. In contrast, voltage loss due to bubble-induced local hydroxide mass transport has the most dominant effect at high current density, which is also the most challenging component to model accurately. As a result, the model slightly over-predicts voltage losses at high current density. Since the operating current density typically does not exceed 0.5 A cm^{-2} for realistic hydrogen generation application,[6] this model can be used for an analytical parametric study, thus saving experimental time and operation cost.

In addition to the baseline operating conditions, the model is also applied to perform calculations at KOH concentrations of 1.0M and 0.2M. For different KOH concentrations, the model assumes that the $K^{eff}_{OH^-}$ varies linearly with its hydroxide concentration. The average experimental results from 3 repeated tests, together with the analytical model predictions, are reported in Figure 8B. It can be observed that the errors for model prediction are within 5% when the current densities are below 0.315 A cm^{-2}, indicating that the trend of the experimental data is well captured by the analytical model.

Similar to the result obtained at 0.4M KOH, the largest discrepancies occur at the highest current density (0.6313 A cm^{-2}) primarily due to the inaccuracy of the computed local ohmic resistance at 0.2 and 1.0M KOH. Unlike the 0.2M and 0.4M KOH conditions, the model under-predicts the voltage at the 1.0M KOH condition. This is most likely due to the over-prediction of $K^{eff}_{OH^-}$, which is assumed to vary linearly with the hydroxide concentration. To obtain a more accurate empirical value for the effective hydroxide ionic conductivity at 1.0 M KOH, a similar study varying the electrode distance, as discussed in section 3.2, will be needed. While the analytical model presented here provides insights into fundamental mechanisms, an in-depth experimental study of the local hydrogen and oxygen bubbles is required to further improve the overall accuracy of the model prediction.

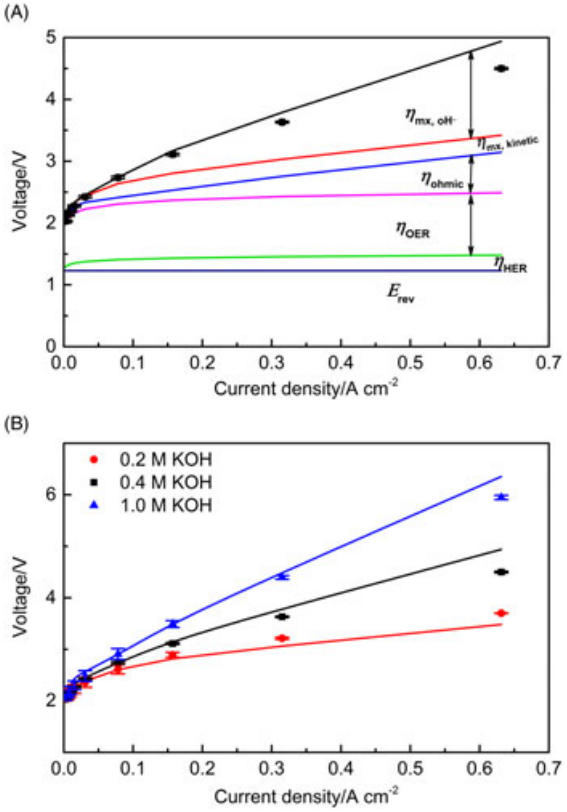

FIGURE 8 Comparison of experimental data (symbols) with analytical modeling results (lines). A, Polarization curves with detail voltage components at 0.4M KOH; B, polarization curves at different KOH concentrations [Colour figure can be viewed at wileyonlinelibrary.com]

4 | CONCLUSIONS

This study has shown, based on experimental results and analytical modeling methodologies, that major over-potentials are caused by OER kinetics and mass transport resistance due to gas bubbles. Compared with cathode HER, OER occurring at the anode has higher Tafel slope and lower exchange current density. Depending on the bubble dynamics, the fitted results indicate that the bulk effective hydroxide ionic conductivity of the 0.4M KOH electrolyte is 0.1333 second cm^{-1} and 0.9650 second cm^{-1} at the low and high current density, respectively. Further analysis shows similar bubble coverage at the anode and cathode, which reaches a steady-state condition at around 0.1 A cm^{-2}. Ultimately, the model predictions for various KOH concentrations show good agreement with experimental results. These findings not only capture all of the fundamental physics but also provide a practical approach to simulate complicated electrolysis reaction. This method provides a framework to study various electrolyzer designs and minimize energy losses.

ACKNOWLEDGEMENTS

The authors would like to thank Professor Ashlie Martini for reviewing our work, Dr Md Opu for his preliminary experimental work, and Professor Pan Mu for supporting Yanan Chen through the "Fundamental Research Funds

for the Central Universities" from Wuhan University of Technology. This work was cosponsored by Aldi Far-IR Products, Inc, University of California, Merced, and GREENPower Program (IIID 2015-09) from Commission on Higher Education – Philippine California Advanced Research Institutes (CHED-PCARI) of the Republic of the Philippines.

REFERENCES

1. Shinagawa T, Takanabe K. Towards versatile and sustainable hydrogen production via electrocatalytic water splitting: electrolyte engineering. *ChemSusChem*. 2017;10:1318-1336.
2. Turner J, Sverdrup G, Mann MK, et al. Renewable hydrogen production. *IntJEnergy Res*. 2008;32:379-407.
3. Gandía LM, Oroz R, Ursúa A, Sanchis P, Diéguez PM. Renewable hydrogen production: performance of an alkaline water electrolyzer working under emulated wind conditions. *Energy Fuel*. 2007;21:1699-1706.
4. Carmo M, Fritz DL, Mergel J, Stolten D. A comprehensive review on PEM water electrolysis. *Int J Hydrogen Energy*. 2013;38:4901-4934.
5. Schalenbach M, Tjarks G, Carmo M, Lueke W, Mueller M, Stolten D. Acidic or alkaline? Towards a new perspective on the efficiency of water electrolysis. *JElectrochemSoc*. 2016;163:F3197-F3208.
6. Zeng K, Zhang D. Recent progress in alkaline water electrolysis for hydrogen production and applications. *Progress in Energy and Combustion Science*. 2010;36:307-326.
7. Zhang D, Zeng K. Status and prospects of alkaline electrolysis. *Hydrogen Science and Engineering: Materials, Processes, Systems and Technology*. 2016;283-308.
8. Allen JB, Larry RF. Electrochemical methods: fundamentals and applications. *Department of Chemistry and Biochemistry University of Texas at Austin, John Wiley & Sons, Inc*. 2001; 156–176.
9. Reier T, Nong HN, Teschner D, Schlögl R, Strasser P. Electrocatalytic oxygen evolution reaction in acidic environments–reaction mechanisms and catalysts. *Advanced Energy Materials*. 2016;
10. Dau H, Limberg C, Reier T, Risch M, Roggan S, Strasser P. The mechanism of water oxidation: from electrolysis via homogeneous to biological catalysis. *ChemCatChem*. 2010;2:724-761.
11. Zhang D, Zeng K. Evaluating the behavior of electrolytic gas bubbles and their effect on the cell voltage in alkaline water electrolysis. *Ind Eng Chem Res*. 2012;51:13825-13832.
12. Olivier P, Bourasseau C, Bouamama PB. Low-temperature electrolysis system modelling: a review. *Renew Sustain Energy Rev*. 2017;78:280-300.
13. Kelouwani S, Agbossou K, Chahine R. Model for energy conversion in renewable energy system with hydrogen storage. *JPower Sources*. 2005;140:392-399.
14. Nagai N, Takeuchi M, Nakao M. Effects of generated bubbles between electrodes on efficiency of alkaline water electrolysis. *JSME International Journal Series B Fluids and Thermal Engineering*. 2003;46:549-556.
15. Vanhanen J, Lund P. Computational approaches for improving seasonal storage systems based on hydrogen technologies. *Int J Hydrogen Energy*. 1995;20:575-585.
16. Henao C, Agbossou K, Hammoudi M, Dubé Y, Cardenas A. Simulation tool based on a physics model and an electrical analogy for an alkaline electrolyser. *J.Power Sources*. 2014;250:58-67.
17. Deshmukh SS, Boehm RF. Review of modeling details related to renewably powered hydrogen systems. *Renew Sustain Energy Rev*. 2008;12:2301-2330.
18. Haynes WM. *CRC Handbook of Chemistry and Physics*. Florida: CRC press; 2014.
19. Yu X, Zhang M, Yuan W, Shi G. A high-performance three-dimensional Ni–Fe layered double hydroxide/graphene electrode for water oxidation. *J Mater Chem A*. 2015;3:6921-6928.
20. Chen L, Dong X, Wang Y, Xia Y. Separating hydrogen and oxygen evolution in alkaline water electrolysis using nickel hydroxide. *Nat Commun*. 2016;7:
21. Nagai N, Takeuchi M, Kimura T, Oka T. Existence of optimum space between electrodes on hydrogen production by water electrolysis. *Int J Hydrogen Energy*. 2003;28:35-41.
22. O'Hayre RP, Cha S, Colella W, Prinz FB. *Fuel Cell Fundamentals*. New York: John Wiley & Sons; 2009:25-167.
23. Shinagawa T, Garcia-Esparza AT, Takanabe K. Insight on Tafel slopes from a microkinetic analysis of aqueous electrocatalysis for energy conversion. *Sci Rep*. 2015;5:13801
24. Newman J, Thomas-Alyea KE. *Electrochemical Systems*. John Wiley & Sons; 2012.
25. Santos D, Sequeira C, Macciò D, Saccone A, Figueiredo J. Platinum-rare earth electrodes for hydrogen evolution in alkaline water electrolysis. *Int J Hydrogen Energy*. 2013;38:3137-3145.
26. Milewski J, Guandalini G, Campanari S. Modeling an alkaline electrolysis cell through reduced-order and loss-estimate approaches. *J.Power Sources*. 2014;269:203-211.
27. Reier T, Oezaslan M, Strasser P. Electrocatalytic oxygen evolution reaction (OER) on Ru, Ir, and Pt catalysts: a comparative study of nanoparticles and bulk materials. *Acs Catalysis*. 2012;2:1765-1772.
28. Zeng K, Zhang D. Evaluating the effect of surface modifications on Ni based electrodes for alkaline water electrolysis. *Fuel*. 2014;116:692-698.
29. Hine F, Murakami K. Bubble effects on the solution IR drop in a vertical electrolyzer under free and forced convection. *J. Electrochem.Soc*. 1980;127:292-297.

SUPPORTING INFORMATION

Additional Supporting Information may be found online in the supporting information tab for this article.

How to cite this article: Chen Y, Mojica F, Li G, Chuang PA. Experimental study and analytical modeling of an alkaline water electrolysis cell. *Int J Energy Res*. 2017;1–9. https://doi.org/10.1002/er.3806